Journal of Oceanology and Limnology

https://doi.org/10.1007/s00343-024-4058-0

Research Paper

Hydrographic control on subsurface chlorophyll maximum in the northern South China Sea in autumn*

Xiang GONG[1, 2], Hui LIU[3], Xun GONG[3, 4, 5, **], Jiyao LIU[1, 2], Huiwang GAO[6, 7, **]

[1] *Qingdao University of Science and Technology, Qingdao 266061, China*

[2] *Qingdao Innovation Center of Artificial Intelligence Ocean Technology, Qingdao 266061, China*

[3] *Institute for Advanced Marine Research, China University of Geosciences, Guangzhou 511462, China*

[4] *State Key Laboratory of Biogeology and Environmental Geology, Hubei Key Laboratory of Marine Geological Resources, China University of Geosciences, Wuhan 430074, China*

[5] *Shandong Provincial Key Laboratory of Computer Networks, Qilu University of Technology (Shandong Academy of Sciences), Jinan 250014, China*

[6] *Qingdao National Laboratory for Marine Science and Technology, Qingdao 266100, China*

[7] *Key Laboratory of Marine Environment and Ecology, Ministry of Education of China, Ocean University of China, Qingdao 266071, China*

Received Feb. 28, 2024; accepted in principle May 8, 2024; accepted for publication Aug. 14, 2024

Abstract As a frequently-observed phenomenon in the northern South China Sea (nSCS), subsurface chlorophyll maximum (SCM) evolution from summer to winter remains unclear, neither the associated hydrographic control. In this study, on the basis of in-situ data of fall-season cruises in 2004–2006, we characterized the depth, thickness and intensity of the SCM in the nSCS using a general Gaussian-function fitting approach, and investigated a linkage to the corresponding ocean vertical buoyance properties. Our results show that the SCM becomes deeper, thicker and less intense offshore-wards in the nSCS during fall seasons. In parallel, a correlation between the SCM variation and mixed layer depth exists in the nSCS, and it becomes pronounced in the shelf region compared to the slope and basin areas in autumn. Physically, once warmer surface ocean and thus stronger thermo-determined stratification, the SCM layer goes deeper and becomes thicker and less intense in the nSCS, especially in the shelf area of the nSCS. Moreover, the impact of water temperatures at deeper layers on the vertical stratification exerts more consequent roles on the spatial variability of SCM, compared to surface temperatures in the nSCS. Specifically, the isotherm line of 22 °C acts as crucial indicator for variations of the SCM in the nSCS during autumns.

Keyword: subsurface chlorophyll maximum (SCM); northern South China Sea (nSCS); autumn season; hydrographic control

1 INTRODUCTION

Biogeochemical change in the South China Sea (SCS), the largest marginal sea of the western North Pacific, has been linked to the coherent climate variability involving Asian monsoons and surface ocean circulations (Liu et al., 2013; Hou et al., 2022). On seasonal scale, variation of chlorophyll-*a* (Chl-*a*) concentration in the surface SCS is predominantly controlled by the variability in monsoon winds. Once after the removal of seasonal cycles, Liu et al. (2013) found that surface Chl *a* showed subdued response to a deepened thermocline under La Niña conditions. On inter-annual time scale, the surface Chl *a* shows a reversed relationship with sea surface temperature (SST) in the SCS (Tseng et al., 2005; Tang et al., 2011). Recently, Hou et al. (2022) illustrated a progressive

* Supported by the Ministry of Science and Technology of the People's Republic of China (No. 2019YFE0125000), the National Natural Science Foundation of China-Shandong Joint Fund (No. U1906215), the National Natural Science Foundation of China (No. 41406010), and partially by the Key Laboratory of Coastal Environmental Processes and Ecological Remediation, Chinese Academy of Sciences Opening Fund (No. 2020KFJJ04)

** Corresponding authors: gongxun@cug.edu.cn; hwgao@ouc.edu.cn

warming in the surface SCS and shallower thermal mixed layer depth (MLD) in the northern SCS (nSCS), determining the lower Chl-*a* concentrations during year 1999 to 2019. Moreover, a further study has projected a lowering of surface-ocean Chl *a* in the future due to the continuous global warming (Wang et al., 2023).

Vertically in the SCS, subsurface chlorophyll maximum (SCM) is a year-round phenomenon (Ning et al., 2004; Chen, 2005; Chen et al., 2006; Liu et al., 2007; Xing et al., 2019). The SCM exists below surface-ocean mixed layer where sun light attenuated from above meets nutrients sourced from the deeper ocean, thus leading to the SCM of maximal values of phytoplankton growth rate (Anderson, 1969; Klausmeier and Litchman, 2001; Cullen, 2015). Depths of the SCM range between 20 and 100 m in the SCS (Chen, 2005; Chen et al., 2006; Lu et al., 2010), while SCM intensities vary from 0.3 to 3.9 mg/m^3 (Ning et al., 2004; Chen, 2005; Chen et al., 2006; Lu et al., 2010). The variations of SCM depth were mainly affected by light attenuation in the nSCS (Gong et al., 2014; Chen and Zhao, 2021; Xu et al., 2022). In general, in the nSCS area, nearly 55% of the total Chl *a* in a water column has been found within the SCM layer (Takahashi and Hori, 1984). Moreover, Lu et al. (2010) illustrated that the primary production in the SCM layer was about 65% of those in the plume and upwelled waters during summer.

Existing studies about the SCM in the nSCS have mainly focused on summer and winter seasons. During summer time, the SCM depth decreased shoreward, while its intensity weakened. This is mainly controlled by the processes of coastal upwelling and regional river plume (Lu et al. 2010). Ke et al. (2012) suggested that MLD should be an important factor influencing the depth on SCM in the nSCS in late summer. Similarly, Xu et al. (2018) suggested the response of Chl-*a* variability to hydrodynamic processes in the same region. Compared to the summer processes, the Project of South East Asia Time-series Study (SEATS) have discovered shallowest and strongest SCM in winters whose depths is about 20–30 m deep and of about 0.9-mg/m^3 Chl-*a* concentration (Chen et al., 2006). On seasonal time scale, the evolution of the SCM in the SCS during summer-to-winter transition time, i.e., the autumn season, remains unsolved. In this study, we thus employed a general Gaussian function to fit vertical Chl-*a* profiles and obtained the spatial distribution of the SCM characteristics in the nSCS during autumn seasons, and discussed the associated physical oceanographic controls.

2 DATA AND METHOD

Geographically, the nSCS is a semi-closed basin of 18°N–23°N, 110°E–121°E, and it interacts with the East China Sea, the open Pacific Ocean and the Sulu Sea via the Taiwan Strait and the Luzon Strait, respectively (Fig.1). Physical oceanography observations have shown that the surface circulation in the nSCS mainly flows from the Taiwan Strait, via the Luzon Strait and southwestwards in winters, distinct from northeastward circulation in summers (Chu et al., 1999). In the nSCS, the Taiwan-Strait inflow delivers cold and high nutrients water, compared to Kuroshio-originated, Luzon-Strait inflow water of

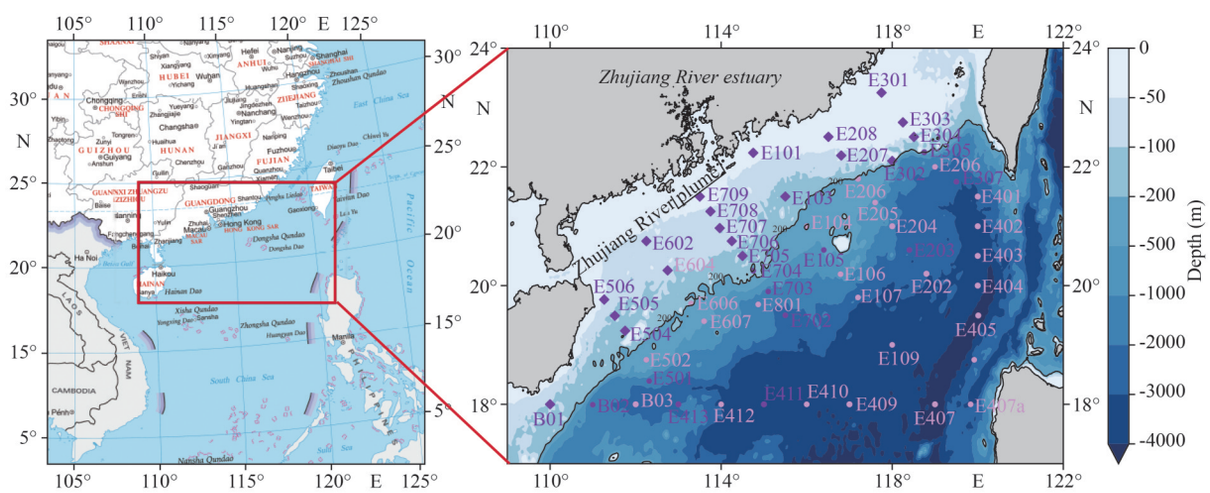

Fig.1 Bathymetry map and sample stations in the northern SCS (nSCS) during 2004–2006 in autumn

Purple dots represent stations with a single sampling, and pink dots represent stations with multiple samplings. Map review No. GS(2022)4314.

relatively warmer, more saline but lower nutrients (Chen, 2003).

2.1 Data source

Our analysis is based on data of 3 cruises in the nSCS of 18.00°N–22.25°N, 110°E–120°E, and in the upper 0–200-m depths (Fig.1). The 3 cruises are proceeded during the fall seasons of 18 September to 2 October 2004, 5–22 September 2005, and 16–27 September 2006. Water samples for Chl-*a* determinations were taken at 0, 10, 25, 50, 75, 100, 150, and 200 m, using a rosette of Niskin bottles attached to a CTD (conductivity-temperature-depth system) probe frame. The observation of Chl-*a* concentrations were fluorometrically determined following acetone extraction of samples collected on GF/F filters, and 4 stations which have only surface Chl *a* were excluded. In total, 65 stations were sampled (see Fig.1), and they are catalogued to 2 sectors according to bathymetries: the continental shelf (depth <200 m), containing 18 stations, and open ocean (depth >200 m, including slope and basin), containing 47 stations.

2.2 Data processing based on Gaussian function

The non-uniform vertical profiles of Chl *a* can be modeled using a shifted-Gaussian function (Lewis et al., 1983) that has subsequently been widely used with small modifications (Platt et al., 1988; Matsumura and Shiomoto, 1993; Gong et al., 2015). Accounting the observed characteristic that surface values always exceed the bottom ones, the shifted-Gaussian functional form is modified with a superimposition of background linearly or exponentially decrease shape along depth (Uitz et al., 2006; Mignot et al., 2011; Gong et al., 2014). Here, we adopted a piecewise function (Gong et al., 2014), which comprises a constant value (P_0) in the surface layer (z_s) and below a shifted-Gaussian function (Eq.1) to approximate the unimodal vertical profiles of Chl *a* (Supplementary Fig.S1). The characteristics of SCM were then derived from the Gaussian parameters.

$$P=\begin{cases} P_0 & 0\le z\le z_s \\ P_{max}\exp\left[-\dfrac{(z-z_m)^2}{2\sigma^2}\right] & z_s<z<z_b \end{cases}, \quad (1)$$

where P is the Chl-*a* concentrations as a function of depth z, P_0 is the Chl *a* above the depth of surface layer (z_s), z_b is the maximum water depth where Chl-*a* concentration can be detected, assumed to be 200 m here. z_s is assumed a constant, which value is set differently in fitting the vertical Chl-*a* profiles. For example, it is set as 10 m in some Chl-*a* profiles over the shelf of the nSCS, 30 m in some profiles in the slope and basin of the nSCS. The three Gaussian parameters (P_{max}, z_m, σ) can characterize the SCM phenomenon (Supplementary Fig.S2), among which P_{max} represents the maximum value of Chl *a* below the surface layer depth z_s, z_m is the depth of the maximum Chl *a* (the peak of the bell shape), and σ is the standard deviation of Gaussian function, which controls the width of the SCM layer. Notably, $P_{max}=h/\left(\sigma\sqrt{2\pi}\right)$, h represents the integral of the Gaussian function (Supplementary Fig.S2). Considering the asymmetrically unimodal distribution of Chl *a* due to the influence of the surface mixed layer, parameter h is not equal to (less than) the total Chl *a* integrated through the water column.

The piecewise equation (Eq.1) is sufficiently versatile to mimic a large variety of vertical Chl-*a* profiles in the nSCS (Supplementary Fig.S3). Within the 95% confidence limits, vertical Chl-*a* profiles that has an R^2>80% accounted for about 75%. That is, out of the 102 profiles, 75 were adequately described by the fitting model, with a significant SCM phenomenon. More specifically, of the 75 profiles, 22 belong to the nSCS shelf region, 10 above continental slope, and 43 from the basin area.

As described in Eq.1, the SCM depth is defined as z_m, that is, the location of the point-wise maximum value of Chl *a* (Supplementary Fig.S2). The SCM intensity refers to the maximum value of Chl *a* (P_{max} in Eq.1) in the water column (Supplementary Fig.S2). The upper and lower boundaries of the SCM layer are defined by the depths where phytoplankton presents maximal gradients, according to $\partial P^2z/\partial^2z=0$ as explained by Beckmann and Hense (2007). Then, we derived the depths that bound the SCM layer from Eq.1, i.e., $z_m-\sigma$ and $z_m+\sigma$, respectively, and the thickness of SCM layer is thereby expressed as 2σ. Furthermore, the boundaries of the SCM layer coincide with the locations of the extrema of the vertical diffusive phytoplankton fluxes $K_v\dfrac{\partial^2P}{\partial z^2}=0$ (K_v is the vertical diffusivity). From a general, one-dimensional phytoplankton equation (Riley et al., 1949; Fennel and Boss, 2003; Beckmann and Hense, 2007; Gong et al., 2015), this alignment results in a balance between the in situ growth rate and all losses,

including the divergence of the sinking flux, respiration, mortality, and grazing in the steady-state version (Supplementary Eq.S1). Therefore, the SCM layer is believed to be a production layer situated between the two compensation depths (Beckmann and Hense, 2007; Gong et al., 2015). Note that the thickness of SCM layer is defined as $z_m+\sigma$ at stations where the upper boundary of SCM layer ($z_m-\sigma$) is less than zero by calculated using the piecewise function (Eq.1).

By compared the SCM depth (z_m) and the surface layer depth (z_s) in the slope and basin of nSCS, we found that the average difference between them is larger than 1.5 times of σ. According to 3-sigma rule of Gaussian function, we calculated the total Chl *a* within 0–200 m (TChl *a*) as following: TChl $a=z_s\times P_0+h$, with unit of mg/m^2. Note that, in the shelf area TChl *a* was estimated from surface to the bottom as following: TChl $a=z_s\times P_0+A\,h$, where parameter A is determined by the distance between the lower boundary of the SCM layer and 200-m water depth. The depth-integrated Chl *a* within the SCM layer (IChl *a*) was then estimated as IChl $a=0.68\times h$ according to the rule of Gaussian function.

3 RESULT AND DISCUSSION

3.1 Spatial variation of SCM characteristics

In our results, the intensity of SCM generally showed an opposite pattern to the SCM bathymetries during fall seasons (Fig.2a). Spatially, the intensity of SCM generally decreases shoreward (Fig.2b). The averaged depth and intensity of SCM are ~41 m, ~0.60 mg/m^3, respectively in the shelf of nSCS, while they turn to deeper and weaker in the slope (~57 m, ~0.37 mg/m^3) and basin (~64 m, ~0.31 mg/m^3) areas. The SCM depths ranged from 40 to 80 m in 78% of the profiles (59 out of 75 vertical Chl-*a* profiles), with an average SCM depth of 58 m (Fig.3a). Extreme values of 10 m and 107 m were observed in isolated instances. Although the SCM intensity ranged from 0.05 to 1.25 mg/m^3, totally 75% (57 out of the 75 vertical Chl-*a* profiles) of the SCM intensity were between 0.25 and 0.55 mg/m^3 and the mode of the distribution was in the 0.37-mg/m^3 range (Fig.3b). An average value of SCM intensity in the nSCS is ~0.40 mg/m^3, thus around 3 times compared to the averaged surface Chl *a* (~0.15 mg/m^3).

The SCM thickness basically increased along depths (Fig.2c). On average, SCM thickness in the shelf of the nSCS was ~41 m, and it was ~48 m and ~52 m in the slope and open ocean areas. Generally, the count distribution show that the thicknesses of SCM ranged between 20 and 60 m, with values <20 m or >60 m occupying 4% and 20% of the total profiles respectively (Fig.3c). Physically, the SCM thickness is influenced by turbulent diffusion, particularly beneath the surface mixed layer (Beckmann and Hense, 2007; Gong et al., 2015). Intense turbulent mixing leads to a greater inflow of nutrients from deep water into the SCM layer, alleviating nutrient constraints and raising its upper boundary. Consequently, the SCM layer thickens with increased levels of turbulent diffusion (Beckmann and Hense, 2007; Gong et al., 2015; Xu

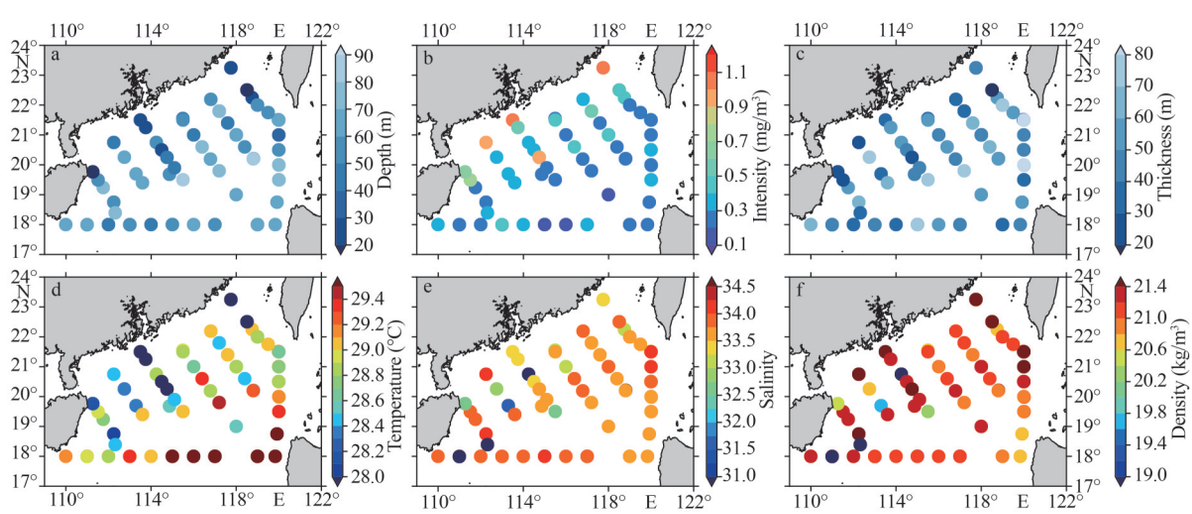

Fig.2 Spatial patterns of SCM characteristics (top panel) (a. depth; b. intensity; c. thickness), spatial patterns of sea surface variables (bottom panel) (d. SST; e. sea surface salinity; f. sea surface density)

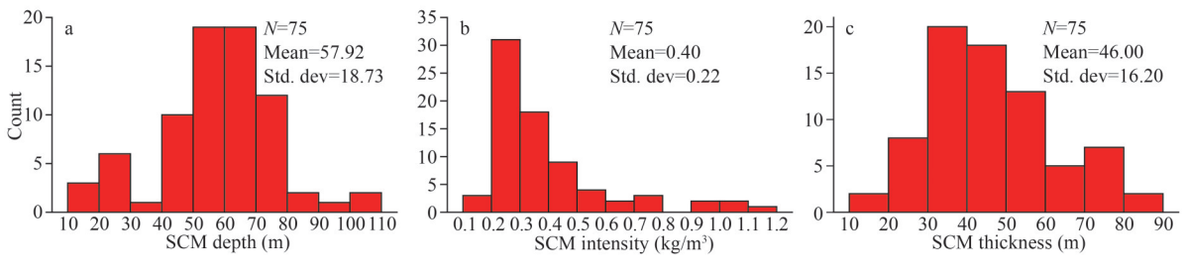

Fig.3 Histogram for the count of SCM depth, intensity and thickness in the nSCS

et al., 2022). In the nSCS along 120°30′E, Yang et al. (2016) revealed that the average turbulent diffusion within the 100–300-m water depth increases as latitude decreases. This increase in turbulent diffusion may partly explain the observed enlargement in SCM thickness offshore from the shelf to the open ocean of the nSCS (Fig.3c). Additionally, light attenuation plays a critical role in affecting SCM thickness (Beckmann and Hense, 2007; Gong et al., 2014, 2015). Moving shoreward in the nSCS, light availability decreases due to increased light attenuation, resulting in less light penetrating into the SCM layer and causing the SCM layer to shrink. The interplay between nutrient dynamics driven by turbulent diffusion and varying light conditions thus explains the spatial variability in SCM thickness across different regions of the nSCS.

As shown in Fig.4a, SCM penetrated deeper accompanies weaker SCM intensity, with a negative correlation of -0.50 (P<0.001), during autumns of year 2004 to 2006. Such linearly fitting relationship is similarly revealed based on logarithmic calculation of SCM depth and SCM intensity (Pearsons' r=-0.50; P<0.001). Moreover, it becomes pronounced in the shelf of nSCS area (Pearsons' r=-0.58; P=0.004, Fig.4a). In comparison, a similar circumstance is similarly revealed for the open ocean of the SCS (Mignot et al., 2011), as well as in other marginal seas of the Bay of Bengal (Murty et al., 2000) and the Southern California Bight (Mantyla et al., 2008). Physically, this is likely controlled by a depth limitation on the SCM intensity due to the exponential decay of solar radiation along depth (Klausmeier and Litchman, 2001; Gong et al., 2015).

Additionally, our analysis reveals an inverse relationship between SCM thickness and its intensity in the nSCS (Pearson's r=-0.56; P<0.001; Fig.4b), meanwhile the SCM thickness presents a positive correlation with its depth (Pearson's r=0.39; P=0.004; Fig.4c). This characterize a circumstance that the SCM becomes weaker and thicker when it goes to a deeper ocean. Physically, it may be partly attributed to reduced light attenuation as one moves offshore (Beckmann and Hense, 2007; Gong et al., 2015; Wang et al., 2020; Chen and Zhao, 2021). Within the shelf region of the nSCS, the SCM thickness does not correlate with the SCM depth (P>0.05, n=22), despite of the remaining significant correlation between the SCM thickness and its intensity (Pearson's r=-0.67; P<0.001; n=22; Fig.4b). The uniqueness of the shelf region, relative to the basin scale, in the nSCS may be caused by the nutrient fluxes due to regional upwelling (Lu et al., 2010; Guo et al., 2017), for instance at stations E304 and E305 (Supplementary Fig.S4). This process enhances SCM intensity and increases SCM

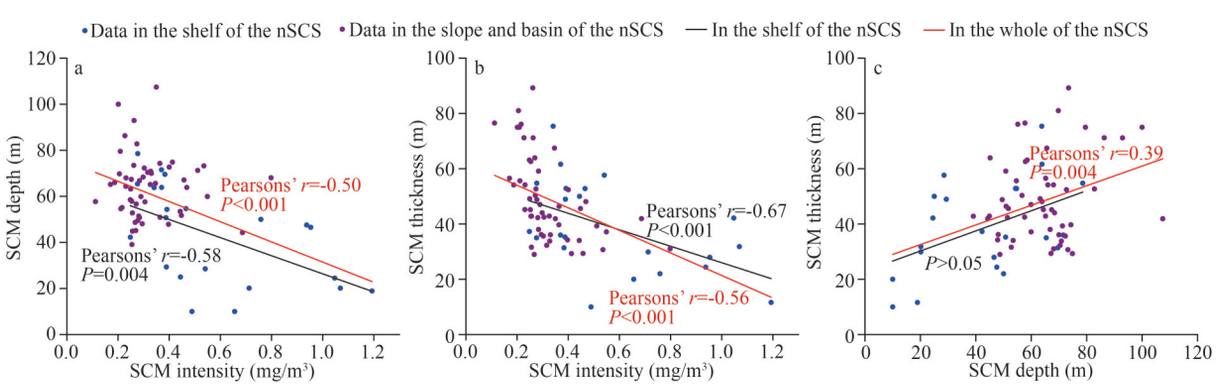

Fig.4 Linear correlations between the sampled (n=75) SCM depth and SCM intensity (a), SCM thickness and its intensity (b), and SCM thickness and its depth (c) in the nSCS

thickness in the shelf area while maintaining a relatively stable depth of the SCM.

3.2 Spatial variation of depth-integrated Chl *a* within the SCM layer

Our results show that surface Chl-*a* concentration in the nSCS spanned between 0.04 and 1.01 mg/m^3. In addition, the mean value of 0.25 mg/m^3 in the shelf area and 0.10 mg/m^3 in the slope and basin of the nSCS are presented, respectively (Fig.5a, squares). The integrated Chl *a* within the SCM layer, IChl *a*, varies between 7.87 and 28.89 mg/m^2, with the averaged value of 13.93 mg/m^2. Spatially, it decreases from the shelf (an averaged value of 17.21 mg/m^2) to the slope and basin regions (an averaged value of 12.58 mg/m^2) (Fig.5b). Similarly, the averaged value of the total Chl *a*, TChl *a*, decreased from 25.31 mg/m^2 in the shelf to 20.90 mg/m^2 in the slope and basin of the nSCS, with a variation range of the TChl *a* between 13.10 and 50.49 mg/m^2 (an averaged value of 22.19 mg/m^2) (Fig.5b). Within the entire nSCS, the IChl *a* contributes to ~63% of TChl *a*. In addition, the proportion of IChl *a* is higher in the shelf of nSCS (71%) than in the slope and basin region (60%).

Both IChl *a* and TChl *a* are correlated to surface Chl *a* commonly in linear fitting relationships (Fig.5c). Moreover, a linear dependence of IChl *a*

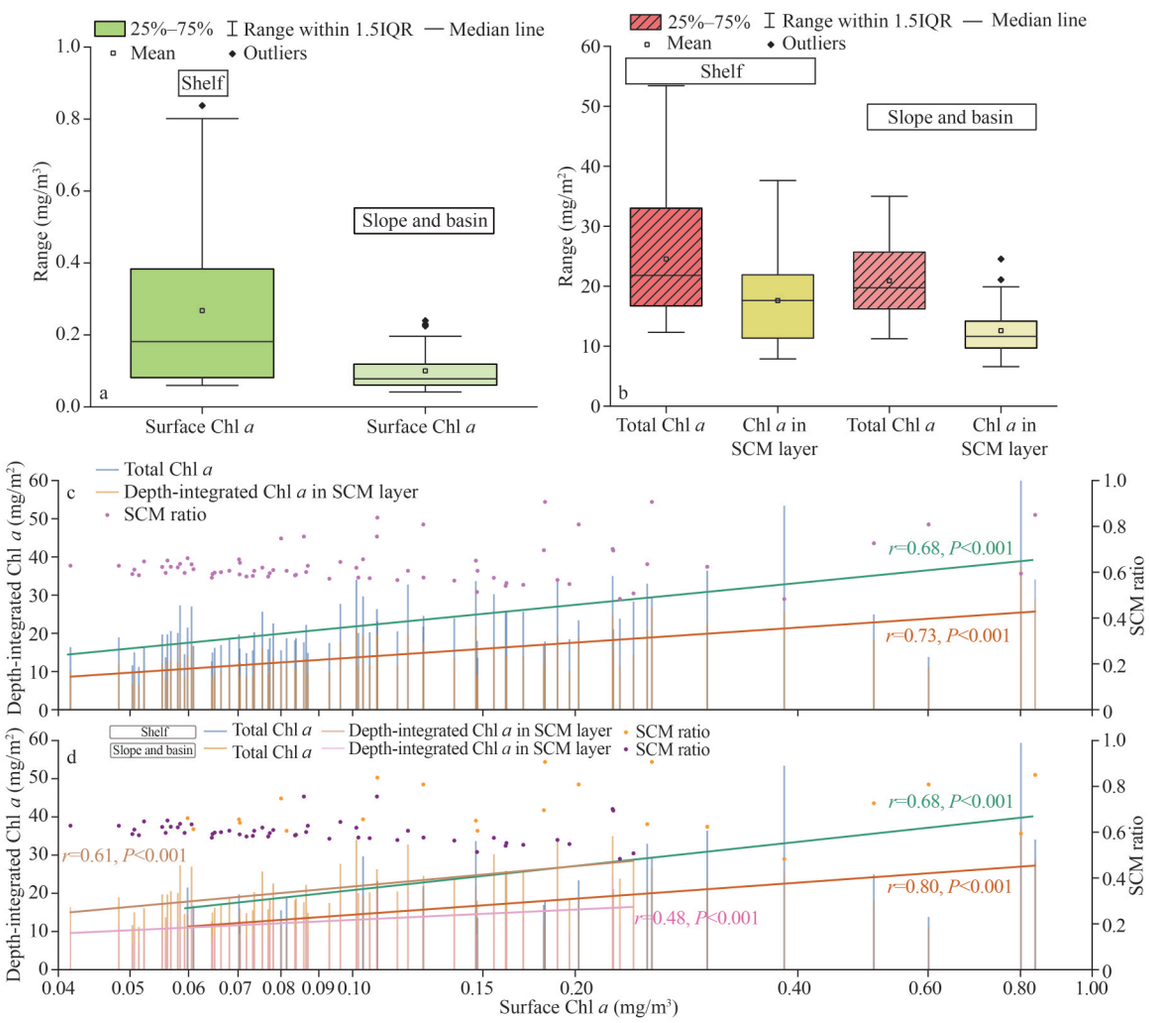

Fig.5 Boxplots of surface Chl *a* (a), total Chl *a* in the water column and depth-integrated Chl *a* in SCM layer (b) in the nSCS and their relationships (c & d)

In (a) and (b), the rectangle represents the interquartile range (25%–75%). The blank lines inside and around the rectangle indicate the median value and 1.5 times interquartile range. In (c) and (d), relationships among total Chl *a* in the water column, depth-integrated Chl *a* in SCM layer, and surface Chl *a* in the whole nSCS (c) and different regions (d). In (c), the green line represents the linear fit for the total Chl *a*, while the red line corresponds to the integrated Chl *a* in the SCM layer for the entire study area. In (d), the green and red lines follow the same conventions as in (c) but for the shelf region, whereas the orange and pink lines represent the slope and basin regions, respectively.

(TChl *a*) on surface Chl-*a* exists in each area of the shelf, slope and basin, respectively (Fig.5d). Spatially, the correlation between depth-integrated Chl *a* and surface Chl *a* slightly increases shoreward, with Pearson's *r* from 0.61 to 0.68 for TChl *a* and from 0.48 to 0.80 for IChl *a*, respectively. This is in line with previous study (Chen and Zhao, 2021) about a significantly positive correlation between surface Chl *a* and depth-integrated Chl *a* within the SCM layer in the nSCS during summer. Furthermore, an integrated Chl *a* within the SCM layer shows variation consistent with Chl *a* within the water column. In parallel, a higher surface Chl-*a* concentration accompanies with a higher values of the Chl *a* both within the SCM layer and the whole water column. Thus, our results suggested that the surface-ocean Chl-*a* concentration may act as an indicator for the depth-integrated Chl *a* at the shelf-sea and open-sea areas.

During September of 2004, 2005, and 2006, sea surface temperatures (SST) across the nSCS exhibited a range of 26.6–29.8 °C (average: 28.8 °C), displaying an upward trend from the shelf to the basin (Fig.2d). Additionally, sea surface salinity and sea surface density exhibited diverse patterns compared to SST, with lower values concentrated near the Zhujiang (Pearl) River plume (Fig.2e–f). SST showed a significant negative correlation with surface Chl *a* in the shelf, while the correlation was relatively weak in the slope and basin during fall (Fig.6a). However, there was no statistically significant correlation among sea surface salinity (or density), surface Chl *a*, and depth-integrated Chl *a* (not shown here). In our results, significant correlations between SST and integrated Chl *a* are primarily observed in the shelf region (P<0.001), while they are not significant in the slope and basin of the nSCS (P>0.1; Fig.6b). Therefore, we assert that SST is an effective indicator for spatial variation in both surface Chl *a* and depth-integrated Chl *a* in the shelf of the nSCS. Nevertheless, it is essential to acknowledge that, for the open ocean, SST cannot be considered a suitable index for depth-integrated Chl *a*, both in the SCM layer and the water column. In contrast to the positive association between surface Chl *a* and depth-integrated Chl *a*, the negative influence of SST on depth-integrated Chl *a* is evident in Fig.5c–d.

In comparison, previous studies have underlined an inverse relationship between the SST and surface Chl *a* across regional to global scales. It suggests that colder SSTs generally indicate a convection situation contributing to elevated nutrients in the surface layer and increased phytoplankton biomass (Behrenfeld et al., 2006; Siegel et al., 2013; Gittings et al., 2018). In a following study, Behrenfeld et al. (2016) cautioned against extrapolating conclusions from the surface layer to depth-integrated production.

Here, we emphasize that the surface Chl *a* could be a better indicator for spatial variations of integrated Chl *a* than SST in the nSCS during fall seasons. Meanwhile, inconsistent relationships among the integrated Chl *a* and SST between the shelf region and the basin implied that the use of SST as a common indicator of phytoplankton biomass dynamics should be performed with caution.

3.3 Influence of surface stratification on SCM

In our results, MLD in the nSCS varies between 14 and 56 m during the autumn sampling periods of 2004–2006, with an average depth of approximately 31 m. Here, our calculation of the MLD is based on

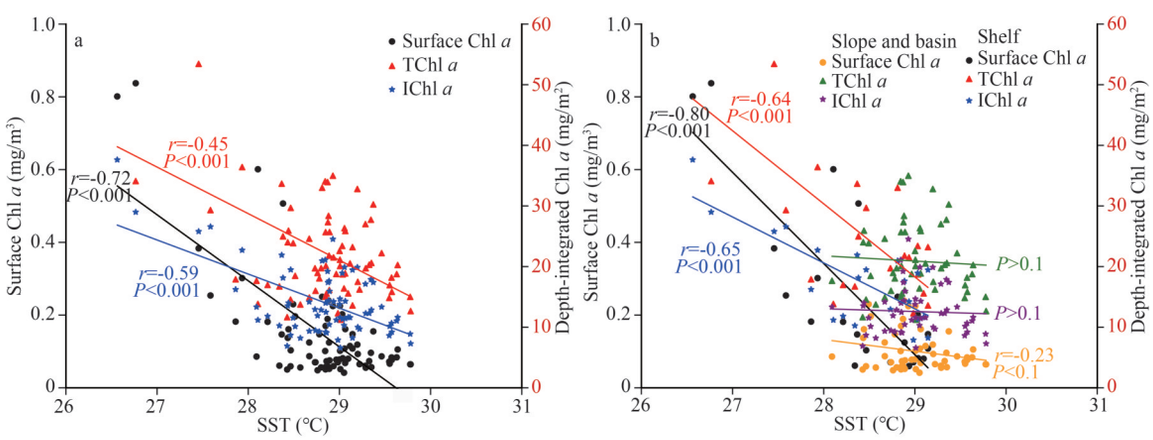

Fig.6 Relationships between SST and surface Chl *a*, IChl *a* (depth-integrated Chl *a* within the SCM layer) and TChl *a* (depth-integrated Chl *a* in total water column) in the nSCS (a) and in the shelf, slope and basin areas of the nSCS (b)

a temperature decrease of 0.2 °C from the 10-m seawater temperature, following the method of Montégut et al. (2004) and aligned with the MLD values calculated by previous studies, e.g., Chen et al. (2005, 2006), Wong et al. (2007). According to previous studies, the MLD deepens during winter in the basin area of nSCS (Tseng et al., 2005; Gong et al., 2014; Xing et al., 2019), even easing the presence of SCM (Liu et al., 2007; Xing et al., 2019). In contrast, SCMs are better established in association with a more stratified upper ocean from spring to autumn in the nSCS (Liu et al., 2007; Xing et al., 2019; Hu et al., 2021). Here, we focus on exploring the correlation of MLD and SCM characteristics during the fall season in the nSCS.

In our results, the SCM depth allocates below the MLD, as suggested by 73% of the total vertical Chl-*a* profiles over the shelf of nSCS (Fig.7a). A significantly positive linear relationship exists between the depth of SCM and MLD, meanwhile the SCM intensity negatively correlates to MLD with R^2=0.21 and P<0.1 (Fig.7b). In parallel, a relatively weaker correlation exists between SCM thickness and MLD (R^2=0.14; P<0.1; Fig.7c). Overall, our results show a dependence of SCM depths, intensity and thickness on the MLD, commonly in the sampling stations of SCM deeper than the corresponding MLD in the shelf of nSCS. In general, a deeper MLD causes the SCM of moving downwards, weaker intensity and enlarged thickness.

According to our analysis, the fitting goodness between MLD and SCM characteristics (depth, intensity, and thickness) reduces to 7%–14% in the slope and basin area of the nSCS, compared to the shelf area (Fig.7d–f). This suggests that when transitioning to open ocean areas, the MLD has relatively less influence on the characteristics of the SCM. It is likely because that the MLD was shallower than the nutricline depth, leading to limited nutrient upwelling from deeper layers into the surface ocean (Chen, 2005; Wong et al., 2007; Xing et al., 2019). Similarly, Beckmann and Hense (2007) showed that the SCM characteristics were retained as long as the MLD is located above the top of the SCM layer in oligotrophic oceans. Here, based on the observations we emphasize that in the slope and basin areas of the nSCS the MLD has minimal influences on SCM characteristics, while in the shelf region the MLD controls variations of SCM depth, at least partially affecting SCM intensity during autumns.

3.4 Response of SCM characteristics to subsurface physical process

Phytoplankton growth is impacted by water temperatures, which can provide a foundation for

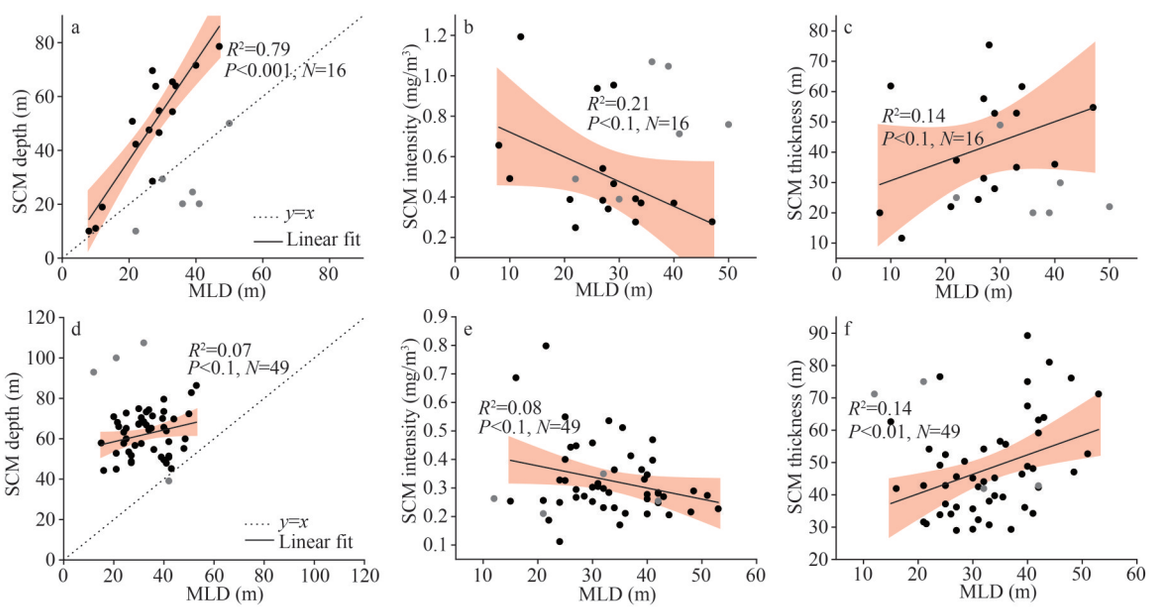

Fig.7 Linear regressions between MLD and SCM characteristics (depth, intensity, and thickness) in the nSCS

For the continental shelf region (a–c) and the combined slope and basin area (d–f), respectively. In the top panel (a–c), the six gray dots were regarded as outliers in the linear regression calculation, which come from stations with MLD deeper than the SCM depth. In the bottom panel (d–f), the four grey dots were regarded as outliers in the linear regression calculation, among which one is from the station with MLD deeper than the SCM depth and the others represent stations with MLD much shallower than the SCM depth. The black line is the linear fit with 95% confidence intervals indicated by pink shading.

modeling the specific growth rate of phytoplankton (Bernard and Rémond, 2012; Grimaud et al., 2017). Additionally, vertical structure of water temperature indirectly affects light and nutrient supplies in the upper ocean by influencing ocean stratifications (Hu and Chen, 2008; Siegel et al., 2013) and the overall growth of phytoplankton, especially within the subsurface layer (Sarmiento et al., 2004). To understand how phytoplankton growth responds to subsurface thermal structure during fall in the nSCS, we examined the relationships between temperatures at different water depths and the SCM characteristics (Fig.8).

Within the nSCS shelf, a positive correlation is evident between SCM depth and SST (Pearson's r= 0.51; P<0.05; Fig.8a). In contrast, a significant negative correlation is observed between SCM depth and temperatures at greater depths (SCM depth and the lower boundary of the SCM layer) (Pearson's r is -0.83 and -0.90, respectively; P< 0.01; Fig.8c–d). The shelf area shows insignificant correlation between the SCM depth and water temperatures at the upper boundary of the SCM layer (P>0.1, Fig.8b). Approaching the slope and basin region, SCM depth correlates with temperatures below the surface layer (Pearson's r is approximately 0.30; P<0.05; Fig.8b–d), except for SST (P>0.1; Fig.8a, top panel).

In the shelf area of the nSCS, the SCM intensity decreases with an increase in SST (Pearson's r= -0.61; P<0.01; Fig.8a), while it deviates from the SCM depth. Moreover, the SCM intensity exhibits an increase along higher temperatures in the subsurface layer (Pearson's r=0.41; 0.52; Fig.8b–c). In comparison, in the slope and basin regions, the SCM intensity becomes solely correlated with water temperature at the upper boundary of the SCM layer (Pearson's r=-0.32; P<0.05; Fig.8b), and has no discernible correlation with temperature at deeper layers (SCM depth and below) (P>0.1; Fig.8a, c, d). Physically, the variation in SCM thickness in the shelf is primarily associated with temperatures at the SCM depth and the lower boundary of the SCM layer (Pearson's r is -0.46, -0.45, respectively; P< 0.05; Fig.8c–d), while in the slope and basin of the nSCS, higher temperatures at the upper layer result in an enlargement of the thickness of the SCM layer (Pearson's r=0.52; P<0.01; Fig.8b).

According to previous studies, higher water temperatures in the upper layer generally enhances vertical stratification, and thus affecting nutrient supply and light penetration (Sharples et al., 2001; Behrenfeld et al., 2006). Such processes could explain the development of deeper and thicker SCMs characterized by a weaker intensity in our results (Fig.8a–b). The control by temperatures from the upper layer to the bottom on the SCM was also discovered in the Arabian Sea (Hu et al., 2021), in which 50 m (at 28 °C) in depth was identified as the threshold where the opposing effects become

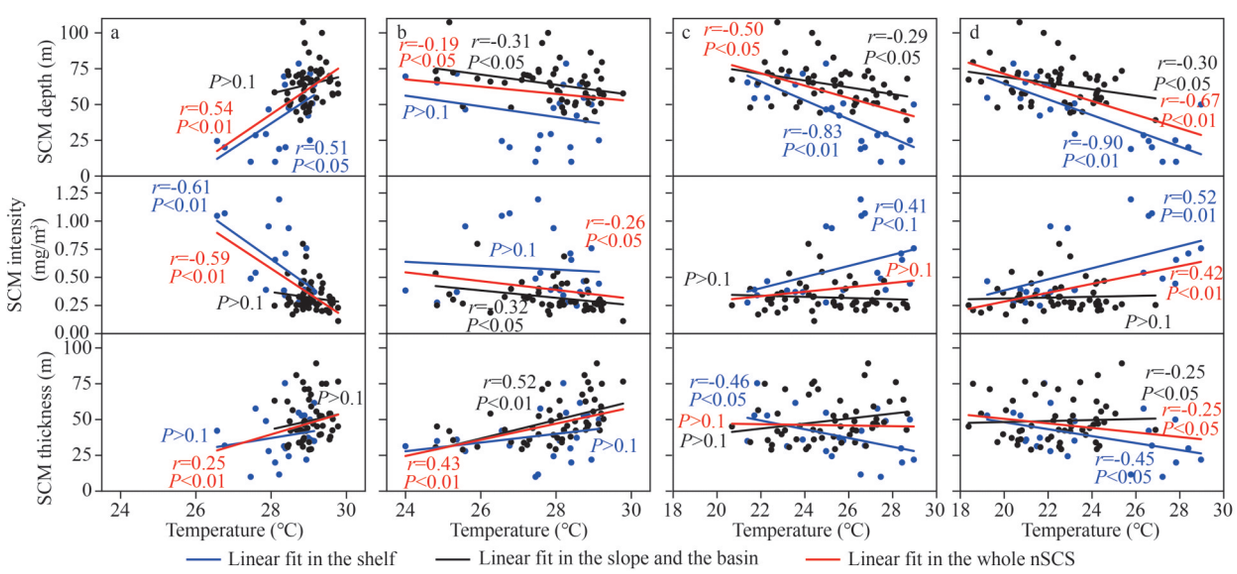

Fig.8 Correlations of SCM characteristics *v.s.* water temperatures at depths

a. SST; b. temperature at the upper boundary of SCM layer; c. temperature at SCM depth; d. temperature at the lower boundary of SCM layer. The red line represents the linear fit of all available data in the nSCS (n=75), the black line represents the linear fit of all available data in the slope and basin area (n= 53), and the blue line is the linear fit of all available data in the shelf area (n=22).

noticeable.

Furthermore, our study revealed a more robust correlation between water temperatures at the deep layer and SCM characteristics, surpassing the correlations observed with water temperature at the upper layer. Once lower water temperatures in deeper ocean, the SCM layer deepens and thins, while the intensity increases (Fig.8c–d). This indicates significant impact of deep mixing processes on shaping SCMs in stratified ocean, similar to observations in the northern North Sea (Zampollo et al., 2023). We then suggest that the bottom of the mixed layer depth is a more reliable predictor of SCM position than surface mixed layer, under the condition of a stratified ocean.

Recent studies have addressed an extrapolation of SCM characteristics across extensive spatial scales by leveraging SST and surface Chl *a* using artificial neural network methods (Sammartino et al., 2018, 2020; Chen et al., 2022; Wang et al., 2023). Here, our results affirm the efficacy of SST and surface Chl *a* as valuable input predictors for such analyses. Moreover, we underscore the superior suitability of incorporating deep-layer water temperature data for an accurate portrayal of vertical Chl-*a* distributions compared to SST in the nSCS.

Additionally, it is observed that water temperatures at the depth of SCMs were consistently higher than 22 °C, with only 6 exceptions (Fig.8c). Thus, previous studies have suggested that the depth of 22-°C isotherm line may serve as a significant indicator for both thermocline depth (Liu et al., 2001; Zhang et al., 2016) and nitricline depth (Xing et al., 2019) in the northern and central South China Sea. Here, we also tested such relationship in the nSCS. According to our analysis, an averaged depth of 22-°C isotherm line was around 86 m and below 25 m from the SCM depth. The significant correlation coefficients obtained during fall in the nSCS were 0.49 (with the SCM depth), -0.30 (with the SCM intensity), and 0.43 (with the SCM thickness), respectively (P<0.01; n=75). This indicates that the shoaling of the 22-°C isotherm tends to entrain more nutrients upwards to invigorate the growth of phytoplankton, ultimately resulting in a shallower, thinner-layer and intensified SCM in the nSCS during the fall season. Here, our results thus highlight the 22-°C isotherm line also as a robust indicator for vertical profiles of Chl *a* in the nSCS. Specifically, a deeper location of the 22-°C isotherm is associated with a deeper, thicker, but weaker SCM layer. This relationship underscores the significant role of subsurface thermal structures in shaping the characteristics of the SCM.

4 SUMMARY

We investigated SCM properties in the nSCS by fitting the vertical Chl-*a* profile using a piecewise function, which comprises a generalized Gaussian function in the subsurface layer and a uniform linear function in the surface layer, and on the basis of observations of 3 cruises during the fall in 2004, 2005, and 2006. In the nSCS, the SCM intensity exhibits a decrease trend, and the SCM depth is gradually increasing from coastal waters to open ocean, with a thicker SCM layer. Statistically, the SCM intensity negatively correlates to the SCM depth and layer thickness. In addition, a positive correlation exists between the SCM thickness and depth. The variation of depth-integrated Chl *a* within the SCM layer is consistent with Chl *a* within the water column, and a higher surface Chl *a* combines a larger Chl *a* both within the SCM layer and the water column. Physically, MLD controls variations of SCM depth, partially influencing SCM intensity in the shelf of the nSCS, but insignificant in the slope and basin area. Once higher SSTs or lower temperatures at lower boundary of SCM layer, the SCM becomes deeper and weaker. With a more significant relationship between the latter and the SCM characteristics, therefore, water temperature at deep layers can be a better proxy as the vertical distribution of subsurface Chl *a* than SST in the nSCS. Dropping displaces of the 22-°C isotherm result in a shallower, thinner SCM layer together with a higher intensity during the fall season. It was underscored the significance of the 22-°C isotherm as a key indicator for understanding variations in SCM characteristics in the nSCS.

5 DATA AVAILABILITY STATEMENT

The datasets generated and/or analyzed during the current study are available from the corresponding author on reasonable request.

6 ACKNOWLEDGMENT

The authors acknowledge the South China Sea Institute of Oceanology, Chinese Academy of Sciences, and National Marine Environmental Forecasting Center, for providing chlorophyll *a* and CTD data. We are very grateful to the anonymous reviewers for the helpful suggestions.

References

Anderson G C. 1969. Subsurface chlorophyll maximum in the northeast Pacific Ocean. *Limnology and Oceanography*, **14**(3): 386-391, https://doi.org/10.4319/lo.1969.14.3.0386.

Beckmann A, Hense I. 2007. Beneath the surface: characteristics of oceanic ecosystems under weak mixing conditions—a theoretical investigation. *Progress in Oceanography*, **75**(4): 771-796, https://doi.org/10.1016/j.pocean.2007.09.002.

Behrenfeld M J, O'Malley R T, Boss E S et al. 2016. Revaluating ocean warming impacts on global phytoplankton. *Nature Climate Change*, **6**(3): 323-330, https://doi.org/10.1038/nclimate2838.

Behrenfeld M J, O'Malley R T, Siegel D A et al. 2006. Climate-driven trends in contemporary ocean productivity. *Nature*, **444**(7120): 752-755, https://doi.org/10.1038/nature05317.

Bernard O, Rémond B. 2012. Validation of a simple model accounting for light and temperature effect on microalgal growth. *Bioresource Technology*, **123**: 520-527, https://doi.org/10.1016/j.biortech.2012.07.022.

Chen C C, Shiah F K, Chung S W et al. 2006. Winter phytoplankton blooms in the shallow mixed layer of the South China Sea enhanced by upwelling. *Journal of Marine Systems*, **59**(1-2): 97-110, https://doi.org/10.1016/j.jmarsys.2005.09.002.

Chen C T A. 2003. Rare northward flow in the Taiwan Strait in winter: a note. *Continental Shelf Research*, **23**(3-4): 387-391, https://doi.org/10.1016/S0278-4343(02)00209-1.

Chen J Q, Gong X, Guo X Y et al. 2022. Improved perceptron of subsurface chlorophyll maxima by a deep neural network: a case study with BGC-Argo float data in the northwestern Pacific Ocean. *Remote Sensing*, **14**(3): 632, https://doi.org/10.3390/rs14030632.

Chen Y, Zhao H. 2021. Spatial distribution of the summer subsurface chlorophyll maximum in the North South China Sea. *PLoS One*, **16**(4): e0248715, https://doi.org/10.1371/journal.pone.024871.

Chen Y L L. 2005. Spatial and seasonal variations of nitrate-based new production and primary production in the South China Sea. *Deep Sea Research Part I*: *Oceanographic Research Papers*, **52**(2): 319-340, https://doi.org/10.1016/j.dsr.2004.11.001.

Chu P C, Edmons N L, Fan C W. 1999. Dynamical mechanisms for the South China sea seasonal circulation and thermohaline variabilities. *Journal of Physical Oceanography*, **29**(11): 2971-2989, https://doi.org/10.1175/1520-0485(1999)029<2971:DMFTSC>2.0.CO;2.

Cullen J J. 2015. Subsurface chlorophyll maximum layers: enduring enigma or mystery solved? *Annual Review of Marine Science*, **7**: 207-239. https://doi.org/10.1146/annurev-marine-010213-135111.

Fennel K, Boss E. 2003. Subsurface maxima of phytoplankton and chlorophyll: steady-state solutions from a simple model. *Limnology and Oceanography*, **48**(4): 1521-1534, https://doi.org/10.4319/lo.2003.48.4.1521.

Gittings J A, Raitsos D E, Krokos G et al. 2018. Impacts of warming on phytoplankton abundance and phenology in a typical tropical marine ecosystem. *Scientific Reports*, **8**(1): 2240, https://doi.org/10.1038/s41598-018-20560-5.

Gong X, Shi J, Gao H W. 2014. Modeling seasonal variations of subsurface chlorophyll maximum in South China Sea. *Journal of Ocean University of China*, **13**(4): 561-571, https://doi.org/10.1007/s11802-014-2060-4.

Gong X, Shi J, Gao H W et al. 2015. Steady-state solutions for subsurface chlorophyll maximum in stratified water columns with a bell-shaped vertical profile of chlorophyll. *Biogeosciences*, **12**(4): 905-919, https://doi.org/10.5194/bg-12-905-2015.

Grimaud G M, Mairet F, Sciandra A et al. 2017. Modeling the temperature effect on the specific growth rate of phytoplankton: a review. *Reviews in Environmental Science and Bio/Technology*, **16**(4): 625-645, https://doi.org/10.1007/s11157-017-9443-0.

Guo L, Xiu P, Chai F et al. 2017. Enhanced chlorophyll concentrations induced by Kuroshio intrusion fronts in the northern South China Sea. *Geophysical Research Letters*, **44**(22): 11565-11572, https://doi.org/10.1002/2017GL075336.

Hou L T, Wang B S, Lai C C et al. 2022. Effects of mixed layer depth on phytoplankton biomass in a tropical marginal ocean: a multiple timescale analysis. *Earth's Future*, **10**(5): e2020EF001842, https://doi.org/10.1029/2020EF001842.

Hu Q W, Chen X Y, He X Q et al. 2021. Effect of El Niño-related warming on phytoplankton's vertical distribution in the Arabian Sea. *Journal of Geophysical Research*: *Oceans*, **126**(11): e2021JC017882, https://doi.org/10.1029/2021JC017882.

Hu Y, Chen J. 2008. Vertical distribution of chlorophyll *a* fluorescence and its response to temperature and salinity near Taiwan Bank in summer. *Journal of Tropical Oceanography*, **27**(2): 18-24. https://doi.org/10.3969/j.issn.1009-5470.2008.02.004. (in Chinese with English abstract)

Ke Z X, Tan Y H, Huang L M et al. 2012. Relationship between phytoplankton composition and environmental factors in the surface waters of southern South China Sea in early summer of 2009. *Acta Oceanologica Sinica*, **31**(3): 109-119, https://doi.org/10.1007/s13131-012-0211-2.

Klausmeier C A, Litchman E. 2001. Algal games: the vertical distribution of phytoplankton in poorly mixed water columns. *Limnology and Oceanography*, **46**(8): 1998-2007, https://doi.org/10.4319/lo.2001.46.8.1998.

Lewis M R, Cullen J J, Platt T. 1983. Phytoplankton and thermal structure in the upper ocean: consequences of nonuniformity in chlorophyll profile. *Journal of Geophysical Research*: *Oceans*, **88**(C4): 2565-2570, https://doi.org/10.1029/JC088iC04p02565.

Liu K K, Chen Y J, Tseng C M et al. 2007. The significance of phytoplankton photo-adaptation and benthic-pelagic coupling to primary production in the South China Sea: observations and numerical investigations. *Deep Sea Research Part II*: *Topical Studies in Oceanography*, **54**(14-15): 1546-1574, https://doi.org/10.1016/j.dsr2.2007.05.009.

Liu K K, Wang L W, Dai M et al. 2013. Inter-annual variation of chlorophyll in the northern South China Sea observed at the SEATS Station and its asymmetric responses to climate oscillation. *Biogeosciences*, **10**(11): 7449-7462, https://doi.org/10.5194/bg-10-7449-2013.

Liu Q Y, Jia Y L, Liu P H et al. 2001. Seasonal and intraseasonal thermocline variability in the central South China Sea. *Geophysical Research Letter*, **28**(23): 4467-4470, https://doi.org/10.1029/2001GL013185.

Lu Z M, Gan J P, Dai M H et al. 2010. The influence of coastal upwelling and a river plume on the subsurface chlorophyll maximum over the shelf of the northeastern South China Sea. *Journal of Marine Systems*, **82**(1-2): 35-46, https://doi.org/10.1016/j.jmarsys.2010.03.002.

Mantyla A W, Bograd S J, Venrick E L. 2008. Patterns and controls of chlorophyll-*a* and primary productivity cycles in the Southern California Bight. *Journal of Marine Systems*, **73**(1-2): 48-60, https://doi.org/10.1016/j.jmarsys.2007.08.001.

Matsumura S, Shiomoto A. 1993. Vertical distribution of primary productivity function phi, 2: for the estimation of primary productivity using by satellite remote sensing. *Bulletin-National Research Institute of Far Seas Fisheries* (*Japan*), (30): 227-270, https://agris.fao.org/search/en/providers/122558. (in Japanese)

Mignot A, Claustre H, D'Ortenzio F et al. 2011. From the shape of the vertical profile of in vivo fluorescence to Chlorophyll-*a* concentration. *Biogeosciences*, **8**(8): 2391-2406, https://doi.org/10.5194/bg-8-2391-2011.

Murty V S N, Gupta G V M, Sarma V V et al. 2000. Effect of vertical stability and circulation on the depth of the chlorophyll maximum in the Bay of Bengal during May-June, 1996. *Deep Sea Research Part I*: *Oceanographic Research Papers*, **47**(5): 859-873, https://doi.org/10.1016/S0967-0637(99)00071-0.

Ning X, Chai F, Xue H et al. 2004. Physical-biological oceanographic coupling influencing phytoplankton and primary production in the South China Sea. *Journal of Geophysical Research*: *Oceans*, **109**(C10): C10005, https://doi.org/10.1029/2004JC002365.

Platt T, Sathyendranath S, Caverhill C M et al. 1988. Ocean primary production and available light: further algorithms for remote sensing. *Deep Sea Research Part A*. *Oceanographic Research Papers*, **35**(6): 855-879, https://doi.org/10.1016/0198-0149(88)90064-7.

Riley G A, Stommel H, Bumpus D F. 1949. Quantitative ecology of the plankton of the western North Atlantic. *Bulletin of the Bingham Oceanographic Collection*, **12**(3): 1-69, https://elischolar.library.yale.edu/bulletin_yale_bingham_oceanographic_collection/64.

Sammartino M, Marullo S, Santoleri R et al. 2018. Modelling the vertical distribution of phytoplankton biomass in the Mediterranean Sea from satellite data: a neural network approach. *Remote Sensing*, **10**(10): 1666, https://doi.org/10.3390/rs10101666.

Sammartino M, Nardelli B B, Marullo S et al. 2020. An Artificial Neural Network to infer the Mediterranean 3D chlorophyll-*a* and temperature fields from remote sensing observations. *Remote*. *Sens*, **12**(24): 4123, https://doi.org/10.3390/rs12244123.

Sarmiento J L, Slater R, Barber R et al. 2004. Response of ocean ecosystems to climate warming. *Global Biogeochemical Cycles*, **18**(3): GB3003, https://doi.org/10.1029/2003GB002134.

Sharples J, Moore M C, Rippeth T P et al. 2001. Phytoplankton distribution and survival in the thermocline. *Limnology and Oceanography*, **46**(3): 486-496, https://doi.org/10.4319/lo.2001.46.3.0486.

Siegel D A, Behrenfeld M J, Maritorena S et al. 2013. Regional to global assessments of phytoplankton dynamics from the SeaWiFS mission. *Remote Sensing of Environment*, **135**: 77-91, https://doi.org/10.1016/j.rse.2013.03.025.

Takahashi M, Hori T. 1984. Abundance of picophytoplankton in the subsurface chlorophyll maximum layer in subtropical and tropical waters. *Marine Biology*, **79**(2): 177-186, https://doi.org/10.1007/BF00951826.

Tang S L, Dong Q, Liu F F. 2011. Climate-driven chlorophyll-*a* concentration interannual variability in the South China Sea. *Theoretical and Applied Climatology*, **103**(1): 229-237, https://doi.org/10.1007/s00704-010-0295-6.

Tseng C M, Wong G T F, Lin I I et al. 2005. A unique seasonal pattern in phytoplankton biomass in low-latitude waters in the South China Sea. *Geophysical Research Letters*, **32**(8): L08608, https://doi.org/10.1029/2004GL022111.

Uitz J, Claustre H, Morel A et al. 2006. Vertical distribution of phytoplankton communities in open ocean: an assessment based on surface chlorophyll. *Journal of Geophysical Research*: *Oceans*, **111**(C8): C08005, https://doi.org/10.1029/2005JC003207.

Wang G F, Zhou W, Xu Z T et al. 2020. Vertical variations in the bio-optical properties of seawater in the northern South China Sea during summer 2008. *Acta Oceanologica Sinica*, **39**(4): 42-56, https://doi.org/10.1007/s13131-020-1535-y.

Wang T H, Sun Y, Su H et al. 2023. Declined trends of chlorophyll *a* in the South China Sea over 2005-2019 from remote sensing reconstruction. *Acta Oceanologica Sinica*, **42**(1): 12-24, http://doi.org/10.1007/s13131-022-2097-y.

Wong G T F, Tseng C M, Wen L S et al. 2007. Nutrient dynamics and N-anomaly at the SEATS station. *Deep Sea Research Part II*: *Topical Studies in Oceanography*, **54**(14-15): 1528-1545, https://doi.org/10.1016/j.dsr2.2007.05.011.

Xing X G, Qiu G Q, Boss E et al. 2019. Temporal and vertical variations of particulate and dissolved optical properties in the South China Sea. *Journal of Geophysical Research*: *Oceans*, **124**(6): 3779-3795, https://doi.org/10.1029/2018JC014880.

Xu W L, Wang G F, Cheng X H et al. 2022. Characteristics of subsurface chlorophyll maxima during the boreal summer in the South China Sea with respect to environmental properties. *Science of the Total Environment*, **820**: 153243, https://doi.org/10.1016/j.scitotenv.2022.153243.

Xu W L, Wang G F, Zhou W et al. 2018. Vertical variability of chlorophyll *a* concentration and its responses to hydrodynamic processes in the northeastern South China Sea in summer. *Journal of Tropical Oceanography*, **37**(5): 62-73, https://doi.org/10.11978/2017121. (in Chinese with English abstract)

Yang Q X, Zhao W, Liang X F et al. 2016. Three-dimensional distribution of turbulent mixing in the South China Sea. *Journal of Physical Oceanography*, **46**(3): 769-788, https://doi.org/10.1175/JPO-D-14-0220.1.

Zampollo A, Cornulier T, O'Hara Murray R et al. 2023. The bottom mixed layer depth as an indicator of subsurface Chlorophyll *a* distribution. *Biogeosciences*, **20**(16): 3593-3611, https://doi.org/10.5194/bg-20-3593-2023.

Zhang W Z, Wang H L, Chai F et al. 2016. Physical drivers of chlorophyll variability in the open South China Sea. *Journal of Geophysical Research*: *Oceans*, **121**(9): 7123-7140, https://doi.org/10.1002/2016JC011983.

SUPPLEMENTARY MATERIALS

$$\frac{\partial P}{\partial t}=\left(\mu-R\right)P-w\frac{\partial P}{\partial Z}+K_{\mathrm{v}}\frac{\partial^2 P}{\partial Z^2}, \tag{S1}$$

where P represents Chl-*a*, t is time, μ is the growth rate, R is the rate of biological losses (including grazing, respiration, and mortality), w is the settling velocity of phytoplankton, and K_{v} is the vertical diffusivity.

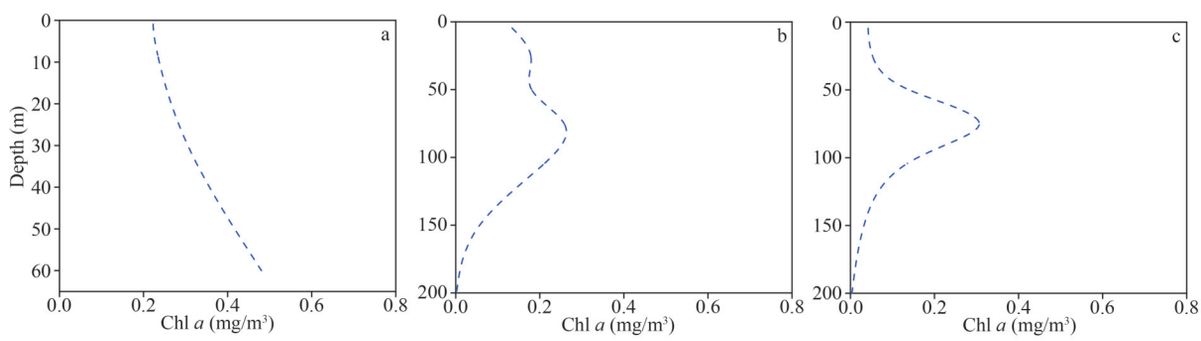

Supplementary Fig.S1 Types of vertical chlorophyll profiles in the nSCS fall

a. increasing type, accounting for 14% of the total profiles; b. bimodal type, accounting for 5% of the total profiles; c. unimodal type, accounted for 81% of the total profiles.

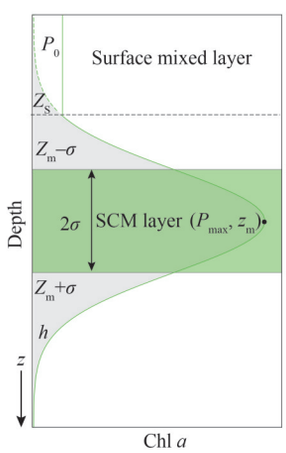

Supplementary Fig.S2 Schematic picture of SCM characteristics (depth, thickness, and intensity)

The green solid line is Chl-*a* concentration as a function of depth, fitted by a piecewise function; the green dot line is part of Gaussian fitting function. Horizontal dashed line represents the depth of surface mixed layer z_s. Horizontal solid lines indicate the locations of the upper and lower SCM layer, $z_m-\sigma$ and $z_m+\sigma$, respectively. z_m is the depth of maximum in Chl-*a* concentrations, i.e., SCM depth. P_{max} indicates the maximum in Chl-*a* concentrations, or SCM intensity. Double arrow represents the thickness of the SCM layer, 2σ. The gray shade and overlapped green shade represent Gaussian parameter h for deriving $P_{max}=h/(\sigma\sqrt{2\pi})$. The green shade indicates the SCM layer.

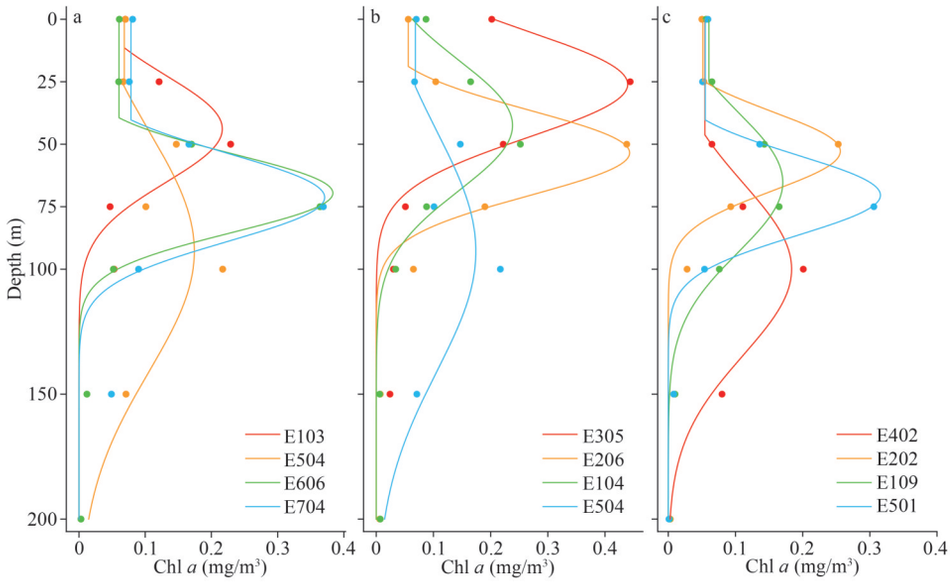

Supplementary Fig.S3 Fitting curves of vertical Chl-*a* profiles by the piecewise function in the shelf (a), the slope (b), and the basin of the nSCS

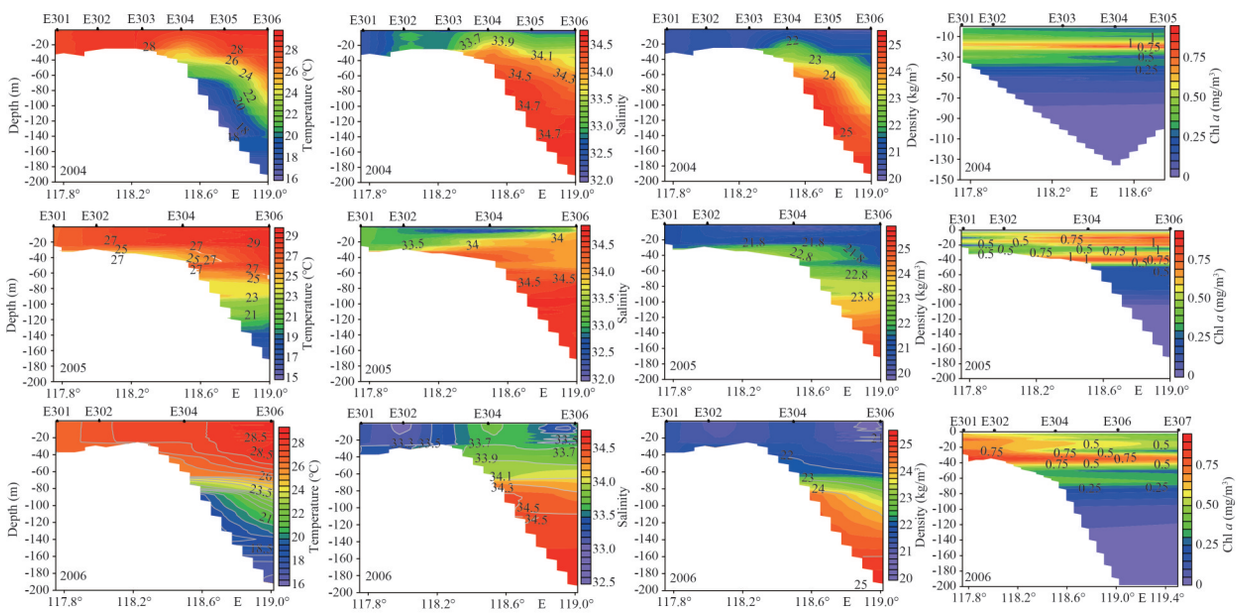

Supplementary Fig.S4 Contours of temperature, salinity, density, and Chl *a* along transection E3 during 2004–2006